RSC Advances

PAPER

View Article Online
View Journal | View Issue

Open Access Article. Published on 14 November 2020. Downloaded on 2/3/2026 10:53:50 PM.
This article is licensed under a Creative Commons Attribution-NonCommercial 3.0 Unported Licence.

Check for updates

Cite this: *RSC Adv.*, 2020, **10**, 41523

A useful preparation of ultrasmall iron oxide particles by using arc plasma deposition†

Yumi Ida,[a] Atsushi Okazawa,‡[b] Kazutaka Sonobe,[c] Hisanori Muramatsu,[c] Tetsuya Kambe,[ac] Takane Imaoka,[ac] Wang-Jae Chun,[d] Makoto Tanabe*[a] and Kimihisa Yamamoto*[ac]

Received 30th August 2020
Accepted 6th November 2020

DOI: 10.1039/d0ra07443h

rsc.li/rsc-advances

Ultrasmall particles, different from the larger size nanoparticles, have recently attracted significant attention in the scientific community in nanotechnology for catalytic, electronic and optical applications; however, their magnetic properties remain unexplored due to the difficult structural analysis. A challenging issue is to develop a preparation method for iron oxide particles (IOPs) with fine size control, and to determine the dependence of magnetic properties on the morphology and crystallinity of the magnetic particles. However, synthetic approaches to obtain IOPs, regarded as one of the new fields of magnetic nanoparticles, have been significantly limited. This article reported a developed synthetic method to prepare IOPs on carbon supports using pulsed arc plasma deposition (APD) in flowing oxygen gas, which clarified the finely-controlled formation of IOPs on graphene nanosheets. Structural characterization of the IOPs revealed the formation of crystalline γ-Fe_2O_3 ultrasmall particles with oxygen deficiency. The pulsed APD method for IOPs is the first simple and convenient technique to not only prevent significant aggregation and contamination by organic compounds and avoid the need for thermal pretreatment, but also provide uniform crystalline nano-order particles.

Introduction

Magnetic iron oxide nanoparticles have attracted significant attention among the scientific community in nanotechnology and biotechnology for applications such as high-density magnetic storage media, magnetocaloric refrigeration and magnetic resonance imaging.[1–3] The advantage of iron oxide nanoparticles relies on their chemical stability and biochemical suitability after the appropriate surface modification, which prevents the aggregation of the particles and provides the functionalization needed for nanomaterials and biomedicine.[4,5] The rich arrangement of iron oxide polymorphs, including magnetite (Fe_3O_4), hematite (α-Fe_2O_3) and maghemite (γ-Fe_2O_3), exhibits unique magnetic properties tuneable by controlling their morphology and crystallinity.[6,7] It is also important to probing the local environment of iron oxide particles in order to understand the magnetic properties depending on intrinsic or native defects.[8,9] The most fundamental synthetic approach for iron oxide nanoparticles, *i.e.*, the coprecipitation method, produces nanosized Fe_3O_4 particles from the mixing of ferrous (Fe^{2+}) and ferric (Fe^{3+}) materials,[10] which are subsequently transformed into thermally stable γ-Fe_2O_3 *via* oxidation and, finally, converted to the most stable form, α-Fe_2O_3 at 450 °C.[11] The synthetic methods for size-controlled iron oxide nanoparticles require careful selection of precursors, control of the temperature, and use of organic templates such as citric and oleic acids.[12–19] However, since the large size nanoparticles to prepare of Fe_3O_4 or γ-Fe_2O_3 may remain mixed after annealing, it is extremely hard to obtain uniform iron oxide particles (IOPs) with tiny sized nanoparticles.

Pulsed arc plasma deposition (APD) is a useful technique for the gram-scale and solvent-free synthesis of size-controlled metallic nanoparticles on various supports under direct and dry conditions, in contrast to the multi-step wet impregnation process.[20,21] The biggest advantage of APD deposition is that it can prevent impurities from being mixed into the nanomaterials and achieve high dispersion of uniform particles on the supports by controlling the APD parameters, *e.g.*, the number of arc plasma pulse shots, the discharge voltage, and the discharge condenser capacitance. The strong adherence of the nanoparticles on the supports due to the high energy

[a]*JST-ERATO, Yamamoto Atom Hybrid Project, Tokyo Institute of Technology, Yokohama 226-8503, Japan. E-mail: yamamoto@res.titech.ac.jp*

[b]*Department of Basic Science, Graduate School of Arts and Sciences, The University of Tokyo, Tokyo 153-8902, Japan*

[c]*Laboratory for Chemistry and Life Science, Tokyo Institute of Technology, Yokohama 226-8503, Japan*

[d]*Graduate School of Arts and Sciences, International Christian University, Mitaka, Tokyo 181-8585, Japan*

† Electronic supplementary information (ESI) available. See DOI: 10.1039/d0ra07443h

‡ Present address: Division of Chemistry, Institute of Liberal Education, Nihon University School of Medicine, Tokyo 173-8610, Japan.

Open Access Article. Published on 14 November 2020. Downloaded on 2/3/2026 10:53:50 PM.
This article is licensed under a Creative Commons Attribution-NonCommercial 3.0 Unported Licence.

discharge causes surface and interfacial anisotropy in the nanoparticles, which enhances electrochemical reactions[22,23] and catalytic oxidation[24–27] catalyzed by noble metals or their alloy nanoparticles. Magnetic Fe–Co alloy nanoparticles with large particle sizes (>3 nm), prepared by a pulsed APD method, formed non-spherical alloy grains with low crystallinity.[28,29] Luo reported that an APD procedure using Fe atoms produced nanoparticles with sizes of 3.1 nm composed of a mixture of metallic Fe(0) and oxidized Fe(II) species due to surface oxidation.[30] Therefore, the APD method has not been established for preparing metal oxide particles with uniform controlled oxidation states and crystalline morphology for oxophilic elements.

In this paper, we describe the first one-step preparation of size-controlled IOPs of highly crystalline γ-Fe_2O_3 using a pulsed APD method with O_2 gas flowing, which are different from the ultrasmall Fe_2O_3 particles prepared by a liquid-phase synthetic method. The deposited particles without the need for an annealing techniques and chemical reagents revealed a single component on a two-dimensional carbon support, and enabled the retention of a particle size of less than 2 nm at high density.

Results and discussion

Fig. 1a and b illustrate the APD process with an oxygen gas flow (100 sccm) under vacuum, forming IOPs on three different carbon supports, *i.e.*, Ketjen-black (KB_m), graphene oxide (GO_m), and graphene nanoplatelets (GNP_m) (*m* represents the shot count number). Discharged Fe^+ ions from an arc plasma gun are immediately oxidized to generate $[FeO_n]^+$ species, followed by landing on the supports and formation of iron oxide particles *via* their collection. A high dispersion of the IOPs was achieved by vigorous stirring of the carbon supports during the APD process. Fig. 1c summarizes the particle size estimated by high-angle annular dark-field scanning transmission electron microscopy (HAADF-STEM) observations and the Fe loading obtained from

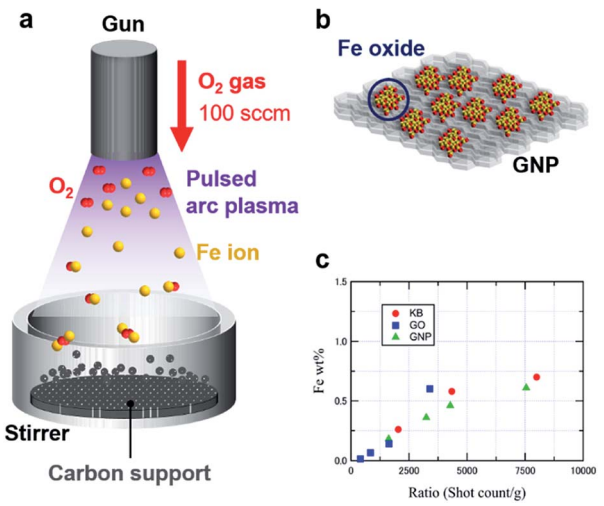

Fig. 1 (a) Process for producing SIOPs using the APD method. (b) Model of the deposited SIOPs on carbon materials. (c) Plots of the Fe loadings *versus* the shot count ratios (shot count/weight of supports: g^{-1}).

Table 1 List of the particle sizes and the Fe loading weight percentages (wt%) *versus* the pulsed shot count

Sample	Shot count	Particle size [nm]	Fe loading [wt%]
KB_{200}	200	1.39 ± 0.20	0.26
KB_{400}	400	2.30 ± 0.65	0.58
KB_{800}	800	3.02 ± 1.00	0.70
KB_{2000}	2000	N/A	2.18
GO_{134}	134	N/A	0.01
GO_{267}	267	0.75 ± 0.16	0.07
GO_{534}	534	1.25 ± 0.21	0.14
GO_{1068}	1068	1.15 ± 0.28	0.60
GNP_{3666}	3666	1.67 ± 0.24	0.18
GNP_{7494}	7494	1.93 ± 0.34	0.36
GNP_{10900}	10 900	1.72 ± 0.50	0.46
GNP_{18409}	18 409	2.48 ± 0.40	0.61
GNP_{20000}	20 000	N/A	1.45

inductively coupled plasma atomic emission spectrometry (ICP-AES) analysis. A linear correlation of the Fe loading to the shot count ratio (shot count/weight of support), which was defined as shot count per mass of the carbon supports, was obtained for all the carbon supports (Tables 1 and S1†).

Fig. 2 shows HAADF-STEM images of the IOPs on the three carbon materials. Iron oxide deposition on KB_{200} produced relatively large particles with diameters of 1.39 ± 0.20 nm, resulting in a low dispersion of the particles on Ketjen-black. Increasing the shot counts (KB_{400} and KB_{800}) produced iron oxide nanoparticles with larger diameters of 2.30 ± 0.65 and 3.02 ± 1.00 nm due to their aggregation (Fig. S1†). In contrast, GO_{267} provided subnano-size particles of 0.75 ± 0.16 nm, together with the landing of single-atom particles on the GO surface. The nucleophilic oxygen atoms on the surface are assumed to cause a strong interaction with the cationic Fe^+ or $[FeO_n]^+$ species. Increasing the shot count by factors of two and four (GO_{534} and GO_{1068}) enlarged the particle sizes to about 1.25 nm (Fig. S2†). High dispersion of the IOPs was also achieved by using supports with a planar morphology with oxygen functional groups on the surface. The GNP were also suitable for deposition of the ultrasmall metal oxide particles with high density and high dispersion. The size of the deposited particle was also controlled in the range between 1.67 ± 0.24 (GNP_{3666}) and 2.48 ± 0.40 (GNP_{18409}) nm, depending on the shot count of the APD process (Fig. S3†). Further increases in the discharge count of Fe^+ ions on GNP gave thin films on the surface (GNP_{20000}; Fig. S4†).

X-ray photoelectron spectroscopy (XPS) measurements of the as-prepared IOPs revealed Fe $2p_{3/2}$ and $2p_{1/2}$ peaks in the range of 710.9–711.5 and 724.1–724.5 eV, respectively (Fig. 3), which are identified as Fe_2O_3 created by oxidation during the APD process, and considering the absence of any metal–support interaction among the three carbon supports (Fig. S5 and S6†). It was difficult to identify the IOPs by X-ray diffraction (XRD), due to low Fe loading amounts.

Fig. 4a shows Fe K-edge X-ray absorption near-edge structure (XANES) spectra of GNP_{10900} (0.46 wt%) and commercially

Open Access Article. Published on 14 November 2020. Downloaded on 2/3/2026 10:53:50 PM.
This article is licensed under a Creative Commons Attribution-NonCommercial 3.0 Unported Licence.

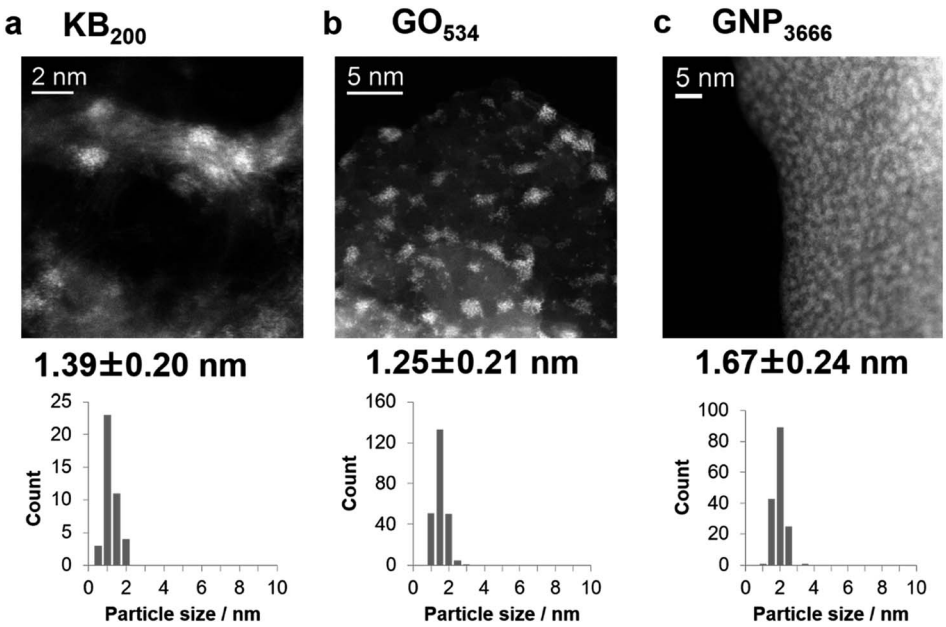

Fig. 2 HAADF-STEM images and particle size histograms of (a) KB_{200}, (b) GO_{534}, and (c) GNP_{3666}.

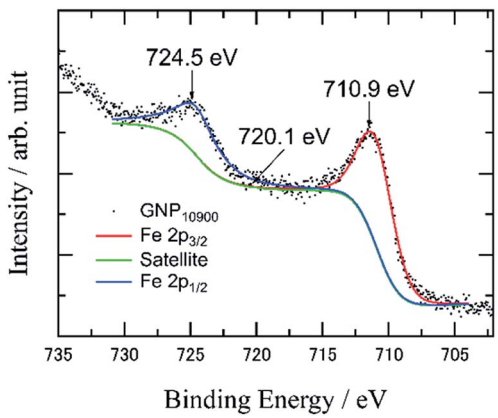

Fig. 3 XPS analysis of GNP_{10900}.

available α-Fe_2O_3, γ-Fe_2O_3 and Fe_3O_4 standards as references. The absorption edge for GNP_{10900} at 7116.0 eV was located between those for 7114.5 eV for Fe_3O_4, with its mixed content of Fe^{2+} and Fe^{3+} species, and ∼7118 eV for α- and γ-Fe_2O_3, which contain iron in the Fe^{3+} state. The weak 1s → 3d pre-edge energy for GNP_{10900} at 7113.2 eV and the dipole-allowed 1s → 4p electron transition feature around 7131.7 eV are similar to the absorption peaks for γ-Fe_2O_3 (7113.1 and 7131.8 eV). The pre-edge curve analysis has been shown to be sensitive to the oxidation state of the iron species. The intensity of the pre-edge peak increases with decreasing coordination number of the iron center due to the loss of inversion symmetry.[31] The γ-Fe_2O_3 structure contains oxygen lattice defects, so the pre-edge peak was analyzed as containing two components with an octahedral FeO_6 geometry (O_h: transition energy from the T_{2g} and E_g orbitals: 7112.6 and 7115.9 eV) and a coordinately unsaturated

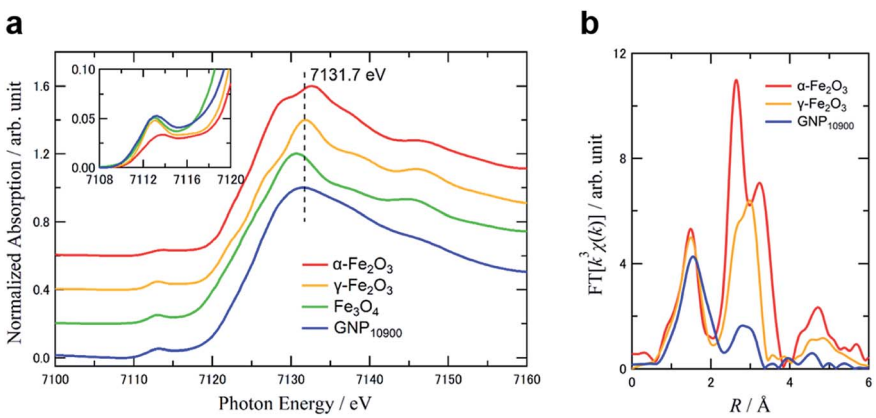

Fig. 4 (a) Normalized XANES spectra of GNP_{10900} (blue), α-Fe_2O_3 (red), γ-Fe_2O_3 (yellow), and Fe_3O_4 (green). Inset shows the pre-edge peaks of all the samples. (b) Fourier transform of EXAFS spectra (k^3: Δk = 3–16 $Å^{-1}$).

Open Access Article. Published on 14 November 2020. Downloaded on 2/3/2026 10:53:50 PM.
This article is licensed under a Creative Commons Attribution-NonCommercial 3.0 Unported Licence.

Table 2 EXAFS analysis data of GNP_{10900}, α-Fe_2O_3, and γ-Fe_2O_3[a]

Sample	N(Fe–O)[b]	r(Fe–O)[c] [Å]	ΔE_0[d] [eV]	$\sigma^2/10^{-3}$[e] [Å]	R_f[f] [%]
α-Fe_2O_3	5.5 ± 0.4	2.06 ± 0.007	1.6 ± 1.4	3.7 ± 0.2	0.034
γ-Fe_2O_3	5.3 ± 0.4	2.05 ± 0.008	3.3 ± 1.5	4.0 ± 0.2	0.039
GNP_{10900}	5.8 ± 0.5	2.10 ± 0.009	6.7 ± 1.5	5.7 ± 0.2	0.039

[a] Fourier transform and Fourier filtering regions for all the samples were limited to Δk = 3.0–16 $Å^{-1}$ and Δr = 0.6–2.2 Å. [b] N, coordination number. [c] r, bond distance between absorber and backscatter atoms. [d] ΔE_0, inner potential correction accounting for the difference in the inner potential between the sample and the reference. [e] σ^2, the Debye–Waller factor (DW). [f] R_f (R-factor), goodness of curve fitting.

tetrahedral FeO_4 geometry (T_d: transition energy from the T_2 orbital: 7113.8 eV). A T_d ratio of 35% was estimated on the basis of the peak areas for T_d and O_h (Fig. S7†). The pre-edge curve fitting for GNP_{10900} exhibited a major component with T_d geometry (7113.4 eV) with a 67% ratio, compared to O_h geometry (7112.0 and 7116.0 eV). The Fourier transform of k^3-weighted EXAFS spectra of GNP_{10900} in the k-space range of 3–16 $Å^{-1}$, as shown in Fig. 4b, were also compared to those of α- and γ-Fe_2O_3. The former peaks for α- and γ-Fe_2O_3 in the first coordination shell (R = 1.0–1.9 Å) were attributed to the direct Fe–O bond. The latter second iron shells (2.1–3.8 Å) were suitable for the assignment of the Fe–Fe or the non-bonding Fe–O distances.[32] The first Fe–O coordination shells for GNP_{10900} was slightly broadened and the magnitude for the second Fe–Fe and the long FeO distances significantly decreased compared to those for the α- and γ-Fe_2O_3 references, resulting from the formation of the IOPs. The curve fit results summarized in Table 2 suggested that the Fe–O bond distance for GNP_{10900} was 2.10 Å, which is slightly longer than the bond distances for the commercially available α- and γ-Fe_2O_3 of 2.06 and 2.05 Å, respectively. The reasonable identification of the small second shell was difficult due to the multicomponent at the surface of the ultrasmall particle.[32] The XAFS results led to the conclusion that the as-prepared GNP_{10900} can be assigned as ultrasmall γ-Fe_2O_3 particles showing an increasing ratio of coordinately unsaturated T_d geometry with decreasing particle size, which is different from the commercially available γ-Fe_2O_3 nanoparticles.

The electronic states of the iron oxides were also confirmed by the electron energy-loss spectroscopy (EELS) spectra of GNP_{20000} with 1.45 wt% film-like iron oxide loading (Fig. S8†). In the Fe L2,3-edge region, the Fe(III) peak at 707.9 eV showed almost the same energy loss for γ-Fe_2O_3, which was different from the full Fe(II) state at 705.9 eV of FeO used as a reference. The spectrum in the O K-edge spectrum was also different from that for the Fe(II) state. Interestingly, the Fe_2O_3 particles of smaller size (GNP_{1500}, 0.29 wt%) showed a Fe(II) peak at 706.5 eV, which could be attributed to reduction from the Fe(III) state due to electron beam exposure during the EELS measurement.

^{57}Fe Mössbauer spectroscopy is very effective at distinguishing iron(III) oxide polymorphs, and also provides an indication of magnetic states, such as superparamagnetism. Fig. 5 shows the Mössbauer spectra for the two samples GNP_{3666} and GNP_{10900}, and the selected parameters of their isomer shift (IS) and quadrupole splitting (QS) are listed along with the data for reported nanoparticles of α- and γ-Fe_2O_3 (Table 3). All the obtained parameters are summarized in Table S2.† The spectra of GNP_{3666} and GNP_{10900} at 300 K display a clearly resolved doublet with IS values of 0.31 and 0.35 mm s^{-1} and QS values of 0.90 and 0.85 mm s^{-1}, respectively, which correspond to the reported values for γ-Fe_2O_3 nanoparticles with an average diameter of 6.5 ± 2.1 nm (IS: 0.33 mm s^{-1}, QS: 0.85 mm s^{-1})[33] rather than those for nanosize α-Fe_2O_3 (IS: 0.30 mm s^{-1}, QS:

Table 3 Fitting parameters of the Mössbauer spectra for GNP_{3666} and GNP_{10900}

Sample	Temp. [K]	IS [mm s^{-1}]	QS [mm s^{-1}]
GNP_{3666}	300	0.31 ± 0.01	0.90 ± 0.02
	10	0.42 ± 0.02	1.02 ± 0.04
GNP_{10900}	300	0.35 ± 0.01	0.85 ± 0.02
	10	0.49 ± 0.02	0.79 ± 0.04
γ-Fe_2O_3[a]	300	0.33	0.85
α-Fe_2O_3[b]	300	0.30	0.68

[a] Particle size: 6.5 ± 2.1 nm.[33] [b] Particle size: <10 nm.[34]

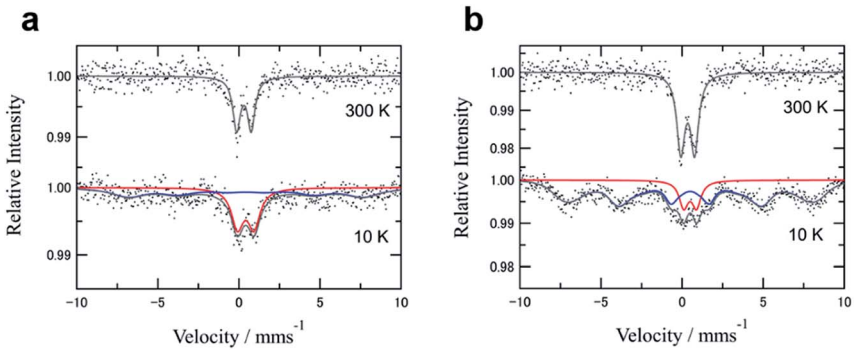

Fig. 5 ^{57}Fe Mössbauer spectra measured of (a) GNP_{3666} and (b) GNP_{10900} at 300 and 10 K. The gray curve denotes the fitting curve, where the red and blue curves stand for the paramagnetic and magnetic components, respectively.

Open Access Article. Published on 14 November 2020. Downloaded on 2/3/2026 10:53:50 PM.
This article is licensed under a Creative Commons Attribution-NonCommercial 3.0 Unported Licence.

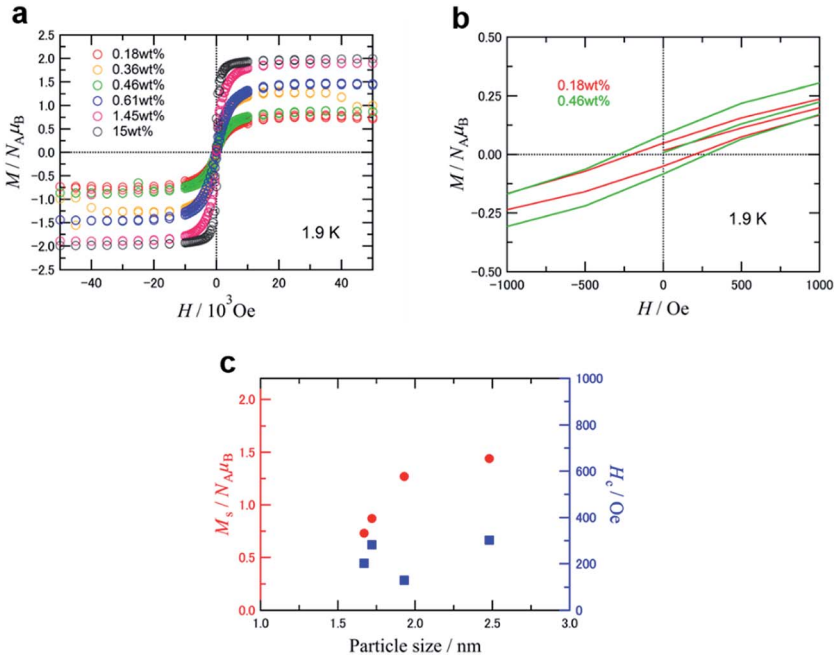

Fig. 6 Magnetization curves for γ-Fe_2O_3 nanoparticles deposited on the GNP series measured at 1.9 K, which indicate the magnetic moments per mole. (a) Magnetization curves ranging from −50 to 50 kOe. (b) Enlarged magnetization curves of GNP_{3666} and GNP_{10900}. (c) Plots of the saturation magnetization (M_s) and coercivity (H_c) for the GNP series *versus* particle size.

0.68 mm s^{-1}).[34] Considering the Néel temperature (T_N = ∼950 K) for the bulk γ-Fe_2O_3 samples, the absence of magnetic components in the spectra is indicative of the nanosize effect, due to faster superparamagnetic relaxation than the Mössbauer time window ($\tau \sim 10^{-9}$). Upon cooling to 10 K, a broadened magnetic sextet appeared in the spectra of both GNP_{3666} and GNP_{10900} in addition to the remaining paramagnetic doublet. The hyperfine field (H_{hyp}) for the sextet reached about 40–45 T, which is slightly smaller than the expected value for the magnetically ordered Fe(III) state. For the 4.6 nm γ-Fe_2O_3 nanoparticles dispersed in polyvinyl alcohol, the magnetic hyperfine splits were completely saturated below 20 K, for which the H_{hyp} extended to ∼50 T.[35] Therefore, the relatively small H_{hyp} and the residual paramagnetic component even at 10 K for GNP_{3666} and GNP_{10900} are attributable to superparamagnetic characteristics, demonstrating a particle size smaller than 4.6 nm, which is consistent with the results of the HAADF-STEM experiments. Additional Mössbauer measurements at various temperatures were hard to perform for GNP_{3666} and GNP_{10900} because of their low Fe-loading concentrations. On the other hand, variable-temperature Mössbauer measurements could be performed for GNP_{20000}, which had a high Fe-loading ratio corresponding to a film-like deposition, affording a rough estimation of the superparamagnetic blocking temperature (for the Mössbauer time-scale) at 120–150 K (Fig. S9†). At 77 K, a paramagnetic doublet and a magnetic sextet also coexisted in the spectrum of GNP_{20000}, which is similar to the spectra of GNP_{3666} and GNP_{10900} at 10 K. Subsequently, the doublet completely disappeared at 10 K in the spectrum of GNP_{20000} to convert the doublet into the sextet. These results rule out the possibility of the presence of another (super)paramagnetic component, as well as any Fe(II) species. Thus, the present nanoparticles prepared on GNP can be assumed to consist of a single component showing superparamagnetism.

Fig. 6a and b show the magnetization curves at 1.9 K for samples of GNP_m with five different Fe loading weights from 0.18 to 1.45 wt%, as well as a reference of commercially available γ-Fe_2O_3 nanoparticles (<50 nm, 15 wt%) mounted on GNP. The saturation magnetization (M_s) per formula unit of Fe_2O_3 and coercivity (H_c) *versus* the particle size are summarized and plotted in Table 4, Fig. 6c and S10.† The temperature dependent magnetization of the GNP_m are shown in Fig. S11.†

The M_s values decreased gradually from 1.44 μ_B to 0.73 μ_B with decreasing particle size from 2.48 nm to 1.67 nm. The sample covered with a thin film of Fe_2O_3 (GNP_{20000}) displayed the highest M_s value (1.89 μ_B), while the H_c value (49 Oe) was the lowest among the five prepared samples. These M_s values are evidently low compared to the ordered magnetic moment of 2.5 μ_B per formula unit for the bulk γ-Fe_2O_3,[36,37] and such a size-dependent M_s decrease has been reported for some

Table 4 Lists of Fe wt%, particle size, M_s and H_c in the GNP series and ≈50 nm γ-Fe_2O_3 purchased nanoparticles

Sample	Fe loading [wt%]	Particle size [nm]	M_s [$N_A\mu_B$]	H_c [Oe]
GNP_{3666}	0.18	1.67 ± 0.24	0.73	202
GNP_{7494}	0.36	1.93 ± 0.34	1.27	129
GNP_{10900}	0.46	1.72 ± 0.50	0.87	282
GNP_{18409}	0.61	2.48 ± 0.40	1.44	302
GNP_{20000}	1.45	N/A	1.89	49
γ-Fe_2O_3	15	≈50	1.99	296

Open Access Article. Published on 14 November 2020. Downloaded on 2/3/2026 10:53:50 PM.
This article is licensed under a Creative Commons Attribution-NonCommercial 3.0 Unported Licence.

nanoparticles of γ-Fe_2O_3 prepared by other methods. This M_s decrease may be caused by the surface spin-canting effect and/or the internal order–disorder effect.[38] The former is derived from spin glass-like behavior in the surface layer, and the latter is attributable to disorder of the Fe-site vacancies in the core to induce some canting of the magnetic moment, that is, M_s appears to be lower due to the imperfectly aligned magnetic moments. The H_c showed less dependence on the particle size, and appeared to be relatively constant (Fig. 6c). Disordered γ-Fe_2O_3 nanoparticles with a size of 2.7–8.7 nm exhibited a large coercivity of 500–1000 Oe at low temperatures,[39] and decreasing particle size resulted in increased coercivity. This indicated the influence of the magnetic interaction between the surface and interior correlated with the particle shape. The magnitude of H_c depends on direct exchange interactions between the internal core spins and the magnetically frozen spins in the disordered surface layer.[38] Therefore, the relatively low H_c for the present samples might be due to their higher crystallinity. The high crystallinity is also supported by the M_s values. The dependence of M_s and the size (4–10 nm) of the iron oxide particles with surface defects indicates that M_s monotonically decreases with particle size.[40] Estimated by extrapolation of the monotonic decrease plot, M_s was 1.3–1.4 μ_B at 2 nm. This M_s value closely corresponds to the value of 1.27 μ_B for GNP_{7494} with low H_c.

To compare the magnetic properties of the IOPs obtained by the APD method, we tried preparing ultrasmall Fe_2O_3 particles by utilizing a liquid-phase synthetic method with a fourth-generation dendritic phenylazomethine (DPA G4) template acting as a ultrasmall-size template (Fig. S12†).[41,42] The $Fe_{60}O_x$@DPA G4/GNP ($GNP_{Fe_{60}}$), prepared from the assembly of 60 eq. of $FeCl_3$ to DPA G4 resulted in a particle size of 1.4 nm and a Fe(III) oxidation state (XPS data: Fe $2p_{3/2}$ = 711.0 eV), which were similar to the values for GNP_{3666} (1.67 nm and 711.1 eV). In contrast, the magnetization curve for $GNP_{Fe_{60}}$ gave a significantly lower value of 0.41 μ_B compared to GNP_{3666} (0.73 μ_B) in spite of the similar particle sizes of $GNP_{Fe_{60}}$ and GNP_{3666}. The enhanced magnetization of the as-deposited GNP_{3666}, compared to the amorphous Fe_2O_3 with a large particle size (~3 nm, 0.57 μ_B)[43] is attributed to the crystallinity of the ultrasmall γ-Fe_2O_3 particles.

Understanding the correlation between the morphology and size of particles and their magnetic parameters is very important for the development of magnetic materials, because magnetic iron oxide particles smaller than 20 nm have been recognized to have superparamagnetic properties. In this study, the APD method achieved the preparation of IOPs of less than 2 nm in size on planar structural graphene supports (GO and GNP), and the characterization results demonstrated the formation of a γ-Fe_2O_3-like structure without annealing at high temperature. For a particle size less than 2 nm, formation of the γ-phase is reasonable because the free energy G is lower than for the other potential phases (ε-, β-, and α-).[44] The oxygen groups of GO serve as an anchor, where the deposited $[FeO_n]^+$ species are favorably adsorbed on the carbon materials, which prevents the migration and aggregation of the particles. In contrast, KB, with a higher specific surface area, exhibited weak adsorption toward the IOPs, enabling the particles to slide off to the edge of the support, promoting aggregation. Fig. 7 shows the models for the formation of IOPs on the carbon materials. Discharged Fe^+ cations are immediately oxidized under flowing oxygen to form $[FeO_n]^+$ species, followed by landing and sliding together on the surface to form iron oxide cores during the initial stage (Fig. 7(1)). The $[FeO_n]^+$ species in the pulsed waves interact with the deposited iron oxide cores, growing pastille-shaped IOPs by stacking the FeO^+ species on the Fe_2O_3 cores (Fig. 7(2)). The driving force for the crystalline γ-Fe_2O_3 particles is attributed to the high deposition energy generated by the pulsed collision, and the landing points are heated by the strong collision of FeO^+ species on the carbon surface. Further shot counts led to occupation of the space on the islands of the iron oxide nanoparticles, providing the particles with higher density and creating large nanoparticles (Fig. 7(3)).

The preparation method for IOPs has a significant effect on the structure and magnetic behavior of particles with similar sizes. The ultrasmall metal oxide synthesized using the DPA template showed amorphous characteristics,[45–48] whereas the IOPs prepared by the gas-phase APD method exhibited high crystallinity. However, the H_c values for the IOPs in the GNP series were smaller than those for the γ-Fe_2O_3 nanoparticles of the same size and/or indicated little size dependence,[38,39] because this difference would largely contribute to the amorphous nature of the particle surface. Increasing the shot count facilitates the vertical stacking of the iron oxide cores (Fig. 7(2)). This is the reason why GNP_{10900} with a larger shot count has smaller particles than GNP_{7494}. The vertically grown IOPs contain a higher amount of surface defects than non-stacked particles of the same size. The defect structures on the surface would lead to enhanced coercivity due to the anisotropic energy being higher than the exchange interaction between the magnetic moments.[38] The geometry of particles grown in-plane direction on carbon nanosheets involves a smaller amount of surface defects than the stacked structure, showing a partially ordered structure. Therefore, H_c decreases and M_s is close to the appropriate value (*e.g.*, GNP_{7494}). In the GNP series, the magnitudes of H_c and M_s are related to the particle shape and the structural distortion on the surface during the particle growth process. For particles growing toward the out-of-plane direction, the surface amorphous content of the particles determines the magnitude of H_c. In contrast, for particles

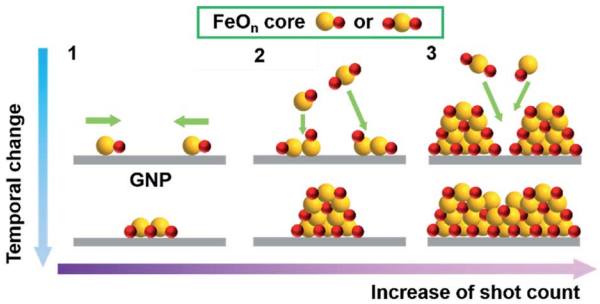

Fig. 7 Model for the growth of iron oxide nanoparticles on GNP. (1) Formation of iron oxide cores, (2) stacking of the FeO^+ species on the Fe_2O_3 cores and (3) growing of the particles with higher density to create large size of the nanoparticles.

Open Access Article. Published on 14 November 2020. Downloaded on 2/3/2026 10:53:50 PM. This article is licensed under a Creative Commons Attribution-NonCommercial 3.0 Unported Licence.

growing toward the in-plane direction, the decrease in the amorphous content leads to an M_s value comparable to that for highly crystalline nanoparticles.

Conclusions

In summary, we demonstrated the preparation of ultrasmall γ-Fe_2O_3-like iron oxide particles on a GNP support without annealing at high temperature. The Fe loadings, obtained from the ICP-AES results, were proportional to the shot count on all the carbon supports. The HAADF-STEM images displayed the presence of IOPs with sizes of less than 2 nm, which were successfully prepared on graphene carbon nanosheets such as GO and GNP. The obtained γ-Fe_2O_3 on GNP was carefully characterized by XPS, Mössbauer, and XAFS spectral analysis. The particle growth on GNP increased two magnetic parameters related to the direction; one is an in-plane direction for M_s and the other is an out-plane direction for H_c. The APD method is useful for the preparation of size-controlled IOPs in the case of graphene derivatives with a two-dimensional structure. The use of GO as a support led to the successful preparation of iron oxide nanoparticles with sizes of about 1 nm even when the Fe loading was increased. The size change for the nanoparticles with Fe loading was also small for the GNP samples. This small change in particle size was characteristic of these graphene analogues with smooth surfaces, unlike the KB series with large particle size changes. Therefore, the use of graphene analogues enabled high-density and high-dispersion deposition while maintaining a small particle size. Moreover, the desired particle size could be achieved by finding the appropriate amount of support. This novel dry process provides a convenient and simple method to synthesize magnetic clusters without annealing.

Experimental section

Materials

All chemical reagents and dehydrated solvents were used without further purification. Dehydrated chloroform was purchased from FUJIFILM Wako Pure Chemical Co. Methanol, dehydrated acetonitrile, and sodium borohydride ($NaBH_4$) were purchased from Kanto Chemical Co., Inc. Iron chloride(III) ($FeCl_3$) and sodium triethylborohydride ($NaBEt_3H$, 1.0 M in toluene) were purchased from Sigma-Aldrich. The iron oxides (α-, γ-) used as the standard samples were purchased from FUJIFILM Wako Pure Chemical Co. and Sigma-Aldrich, respectively. The carbon supports, graphene oxide (GO) and graphene nanoplatelets (GNP) were purchased from Sigma-Aldrich, and Ketjen-black (KB) was obtained from Lion Specialty Chemicals Co., Ltd. The carbon supports were pretreated to remove metallic impurities, with the following procedure described as representative. GNP (2.5 g) was washed with an HCl aqueous solution (300 mL, 3 mol L^{-1}) under ultrasonication for 2 h, followed by filtration and washing with ultrapure water. The GNP was then washed with methanol (100 mL) and dried *in vacuo* at 200 °C immediately before use. A fourth-generation phenylazomethine dendrimer with a tetraphenylmethane core (DPA G4) was synthesized according to a previously reported method.[49]

Overview of experimental and measurement equipment

The IOPs on carbon supports were prepared using an APD-P instrument (Advance Riko, Inc.). The prepared IOPs were characterized by inductively coupled plasma atomic emission spectroscopy (ICP-AES; ICPS-8100, Shimadzu Co.), X-ray photoelectron spectroscopy (XPS; ESCA-3400, Shimadzu Co. and, spectra analysis by using Igor macro[50]), X-ray absorption fine structure (XAFS, BL12C, KEK), Mössbauer spectroscopy (Model 220; Topologic Systems), and high-angle annular dark-field scanning transmission electron microscopy (HAADF-STEM; JEM-ARM200F, JEOL, Ltd.) operated at 80 kV. The electron energy-loss spectroscopy (EELS; GIF Quantum ER, Gatan, Inc.) was performed using a NEOARM atomic resolution TEM system (JEOL Ltd.) with an accelerating voltage of 60 kV. The magnetization measurements were performed using a SQUID magnetometer (MPMS-XL5, Quantum Design, Inc.).

Arc plasma deposition (APD) method

The IOPs supported on KB, GO and GNP were prepared using a pulsed APD method under reduced pressure (0.9 Pa). These carbon materials were stirred in a cup during the deposition process, and IOPs were continuously formed at an oxygen gas flow rate of 100 sccm. The discharge voltage was 100 V, and the discharge count was varied from 134 to 20 000 shots to deposit Fe from 0.18 to 2.18 wt%. These samples were labeled according to the shot count for each carbon support; *e.g.*, KB_{200}, the support was Ketjen-black deposited with 200 shots. The others are the same as described.

XAFS measurements

XAFS was measured in a transmission mode at the BL12C beamlines at the High Energy Accelerator Research Organization Institute of Materials Structure Science Photon Factory (KEK-IMSS-PF). Synchrotron radiation from the storage ring was monochromatized with Si(111) channel-cut crystals. The angle of the monochromator was calibrated using Fe foil. The ionization chambers, as detectors to monitor the incident (I_0) and transmitted X-rays (I), were filled with N_2 and 15% Ar–85% N_2 mixed gas for the Fe K-edge XAFS, respectively. All measurements were conducted at room temperature. The 1s → 3d pre-edge curve analysis was carried out by using XANES dactyloscope freeware.[51] EXAFS curve fitting results were obtained by using REX2000 package (Rigaku Co., Japan). The theoretical phase shifts and the amplitude functions for Fe–O used in the fitting routine were calculated on the basis of the commercially available α-Fe_2O_3 powder.

^{57}Fe Mössbauer spectroscopy

The ^{57}Fe Mössbauer spectra were measured using a conventional Mössbauer spectrometer (Topologic Systems) in transmission mode with a ^{57}Co/Rh γ-ray source. Low-temperature measurements were performed using a CryoMini/CryoStat

Open Access Article. Published on 14 November 2020. Downloaded on 2/3/2026 10:53:50 PM. This article is licensed under a Creative Commons Attribution-NonCommercial 3.0 Unported Licence.

cryogenic refrigerator (Iwatani Industrial Gases Corp.). The samples were placed in a copper holder and the spectra were calibrated using α-Fe foil as a reference at room temperature. Spectral fitting was carried out using the MossWinn 4.0 program.[52]

Magnetic properties

Magnetization curves were measured using a Quantum Design SQUID magnetometer (MPMS-XL5) from −50 to 50 kOe at 1.9 K. The samples were held in a gelatin capsule. The iron oxide nanoparticles supported on GNP were fixed in a small amount of *n*-eicosane due to the high magnetic field during the measurements. The temperature was increased at 320 K to melt the *n*-eicosane. The magnetic responses were corrected with diamagnetic blank data for the sample holder, such as the gelatin capsule, GNP, and *n*-eicosane. The essential data were subtracted from the diamagnetic blank, which is the net weight of GNP from the ICP-AES analysis results.

Liquid-phase synthesis of $Fe_{60}O_x$@DPA G4/GNP

The liquid-phase procedure was performed in an inert-gas-filled glove box. To the mixed solution (95 mL, acetonitrile : chloroform = 1 : 1) containing DPA G4 (3.2 mg, 3.0 μmol L^{-1}), 60 eq. of $FeCl_3$ in acetonitrile solution (5.4 μL, 3.2 mmol L^{-1}) was added. The solution changed from light yellow to dark yellow, and was stirred for 0.5 h. Excess $NaBH_4$ in methanol (3240 μL, 0.30 mol L^{-1}) was added dropwise to the $FeCl_3$–DPA G4 solution for chemical reduction to form dendrimer-encapsulated Fe_{60} particles (Fe_{60}@DPA G4). To the solution of Fe_{60}@DPA G4, GNP (210 mg) dispersed in acetonitrile (50 mL) was immediately added, then the mixture was stirred for 2 h for immobilization. The heterogeneous suspension was oxidized by air exposure and further stirred for 1.5 h. The solvent was partly evaporated and the immobilized support was filtered off, washed with methanol, and dried *in vacuo* overnight to yield $Fe_{60}O_x$@DPA G4/GNP.

Conflicts of interest

There are no conflicts to declare.

Acknowledgements

This study was supported by JST ERATO Grant Numbers JPMJER1503, Japan (K. Y.), Grant-in-Aid for Scientific Research (S) KAKENHI 15H05757 (K. Y.), and Grant-in-Aid for Early-Career Scientists, KAKENHI 18K14084 (Y. I.). The authors are thankful to Mr H. Tanaka (Advance Riko, Inc.) for preparation of the IOPs on carbon supports and Ms M. Morita for her support during the STEM-EELS experiments. The authors also thank our colleagues in the Suzukakedai Materials Analysis Division, Technical Department, Tokyo Institute of Technology, for performing ICP analysis. XAFS measurements were conducted at the BL12C beamlines of the High Energy Accelerator Research Organization—Institute of Materials Structure Science—Photon Factory (KEK-IMSS-PF) under the approval of the Photon Factory Advisory Committee (Proposal numbers 2019G655 and 2019G089).

References

1 D. Ling, N. Lee and T. Hyeon, *Acc. Chem. Res.*, 2015, **48**, 1276–1285.
2 W. Wu, Z. Wu, T. Yu, C. Jiang and W.-S. Kim, *Sci. Technol. Adv. Mater.*, 2015, **16**, 023501.
3 W. Wu, C. Z. Jiang and V. A. L. Roy, *Nanoscale*, 2016, **8**, 19421–19474.
4 N. Zhu, H. Ji, P. Yu, J. Niu, M. U. Farooq, M. W. Akram, I. O. Udego, H. Li and X. Niu, *Nanomaterials*, 2018, **8**, 810.
5 W. Ling, M. Wang, C. Xiong, D. Xie, Q. Chen, X. Chu, X. Qiu, Y. Li and X. Xiao, *J. Mater. Res.*, 2019, **34**, 1828–1844.
6 R. M. Cornell and U. Schwertmann in *The iron oxides: structure, properties, reactions, occurrences and uses*, Wiley-VCH, Weinheim, 2nd edn, completely revised and extended edition, 2003.
7 S. Laurent, D. Forge, M. Port, A. Roch, C. Robic, L. Vander Elst and R. N. Muller, *Chem. Rev.*, 2008, **108**, 2064–2110.
8 J.-M. Li, A. C. H. Huan, L. Wang, Y.-W. Du and D. Feng, *Phys. Rev. B: Condens. Matter Mater. Phys.*, 2000, **61**, 6876–6878.
9 J.-M. Li, X.-L. Zeng and Z.-A. Xu, *Appl. Phys. Lett.*, 2013, **103**, 232410.
10 R. Massart, *IEEE Trans. Magn.*, 1981, **17**, 1247–1248.
11 H. Shokrollahi, *J. Magn. Magn. Mater.*, 2017, **426**, 74–81.
12 W. Wu, Q. He and C. Jiang, *Nanoscale Res. Lett.*, 2008, **3**, 397–415.
13 M. I. Dar and S. A. Shivashankar, *RSC Adv.*, 2014, **4**, 4105–4113.
14 J. Park, K. An, Y. Hwang, J.-G. Park, H.-J. Noh, J.-Y. Kim, J.-H. Park, N.-M. Hwang and T. Hyeon, *Nat. Mater.*, 2004, **3**, 891–895.
15 P. Guardia, A. Labarta and X. Batlle, *J. Phys. Chem. C*, 2011, **115**, 390–396.
16 A. Demortière, P. Panissod, B. P. Pichon, G. Pourroy, D. Guillon, B. Donnio and S. Bégin-Colin, *Nanoscale*, 2011, **3**, 225–232.
17 H. Yun, X. Liu, T. Paik, D. Palanisamy, J. Kim, W. D. Vogel, A. J. Viescas, J. Chen, G. C. Papaefthymiou, J. M. Kikkawa, M. G. Allen and C. B. Murray, *ACS Nano*, 2014, **8**, 12323–12337.
18 Z. Cheng, Q. Fu, H. Duan, Z. Cui, Y. Xue and W. Zhang, *Ind. Eng. Chem. Res.*, 2019, **58**, 8418–8425.
19 S. Kamali, C. J. Chen, B. Bates, C. E. Johnson and R. K. Chiang, *J. Phys.: Condens. Matter*, 2020, **32**, 015302.
20 S. Hinokuma, S. Misumi, H. Yoshida and M. Machida, *Catal. Sci. Technol.*, 2015, **5**, 4249–4257.
21 S. H. Kim, S.-Y. Moon and J. Y. Park, *Top. Catal.*, 2017, **60**, 812–822.
22 S. Takahashi, N. Takahashi, N. Todoroki and T. Wadayama, *ACS Omega*, 2016, **1**, 1247–1252.
23 S. Takahashi, H. Chiba, T. Kato, S. Endo, T. Hayashi, N. Todoroki and T. Wadayama, *Phys. Chem. Chem. Phys.*, 2015, **17**, 18638–18644.

Open Access Article. Published on 14 November 2020. Downloaded on 2/3/2026 10:53:50 PM.
This article is licensed under a Creative Commons Attribution-NonCommercial 3.0 Unported Licence.

24 T. Fujitani, I. Nakamura, T. Akita, M. Okumura and M. Haruta, *Angew. Chem., Int. Ed.*, 2009, **48**, 9515–9518.
25 M. Sadakiyo, S. Yoshimaru, H. Kasai, K. Kato, M. Takata and M. Yamauchi, *Chem. Commun.*, 2016, **52**, 8385–8388.
26 S. M. Kim, H. Lee, K. C. Goddeti, S. H. Kim and J. Y. Park, *J. Phys. Chem. C*, 2015, **119**, 16020–16025.
27 H. Yoshida, S. Misumi, A. Matsumoto, Y. Kuzuhara, T. Sato, J. Ohyama and M. Machida, *Catal. Sci. Technol.*, 2019, **9**, 2111–2117.
28 D. Horiyama, M. Matsuura, T. Yamamoto, N. Tezuka and S. Sugimoto, *Mater. Trans.*, 2016, **57**, 207–211.
29 M. Sadakiyo, M. Heima, T. Yamamoto, S. Matsumura, M. Matsuura, S. Sugimoto, K. Kato, M. Takata and M. Yamauchi, *Dalton Trans.*, 2015, **44**, 15764–15768.
30 X. Luo, J. Lu, E. Sohm, L. Ma, T. Wu, J. Wen, D. Qiu, Y. Xu, Y. Ren, D. J. Miller and K. Amine, *Nano Res.*, 2016, **9**, 1913–1920.
31 T. E. Westre, P. Kennepohl, J. G. DeWitt, B. Hedman, K. O. Hodgson and E. I. Solomon, *J. Am. Chem. Soc.*, 1997, **119**, 6297–6314.
32 J. Zhao, F. E. Huggins, Z. Feng, F. L. Lu, N. Shah and G. P. Huffman, *J. Catal.*, 1993, **143**, 499–509.
33 Sarveena, J. M. Vargas, D. K. Shukla, C. T. Meneses, P. M. Zélis, M. Singh and S. K. Sharma, *Phys. Chem. Chem. Phys.*, 2016, **18**, 9561–9568.
34 W. Kündig, H. Bömmel, G. Constabaris and R. H. Lindquist, *Phys. Rev.*, 1966, **142**, 327–333.
35 E. Tronc, A. Ezzir, R. Cherkaoui, C. Chanéac, M. Noguès, H. Kachkachi, D. Fiorani, A. M. Testa, J. M. Grenèche and J. P. Jolivet, *J. Magn. Magn. Mater.*, 2000, **221**, 63–79.
36 J. M. D. Coey, *Phys. Rev. Lett.*, 1971, **27**, 1140–1142.
37 H. Batis-Landoulsi and P. Vergnon, *J. Mater. Sci.*, 1983, **18**, 3399–3403.
38 M. P. Morales, S. Veintemillas-Verdaguer, M. I. Montero, C. J. Serna, A. Roig, L. Casas, B. Martínez and F. Sandiumenge, *Chem. Mater.*, 1999, **11**, 3058–3064.
39 D. Fiorani, A. M. Testa, F. Lucari, F. D'Orazio and H. Romero, *Phys. B*, 2002, **320**, 122–126.
40 S. R. Cooper, L. K. Plummer, A. G. Cosby, P. Lenox, A. Jander, P. Dhagat and J. E. Hutchison, *Chem. Mater.*, 2018, **30**, 6053–6062.
41 K. Yamamoto and T. Imaoka, *Acc. Chem. Res.*, 2014, **47**, 1127–1136.
42 K. Yamamoto, T. Imaoka, M. Tanabe and T. Kambe, *Chem. Rev.*, 2020, **120**, 1397–1437.
43 L. Machala, R. Zboril and A. Gedanken, *J. Phys. Chem. B*, 2007, **111**, 4003–4018.
44 S. Sakurai, A. Namai, K. Hashimoto and S. Ohkoshi, *J. Am. Chem. Soc.*, 2009, **131**, 18299–18303.
45 Y. Inomata, K. Albrecht and K. Yamamoto, *ACS Catal.*, 2018, **8**, 451–456.
46 Y. Inomata, K. Albrecht, N. Haruta and K. Yamamoto, *Chem. Mater.*, 2019, **31**, 8373–8382.
47 A. Kuzume, M. Ozawa, Y. Tang, Y. Yamada, N. Haruta and K. Yamamoto, *Sci. Adv.*, 2019, **5**, 1–8.
48 K. Sonobe, M. Tanabe and K. Yamamoto, *ACS Nano*, 2020, **14**, 1804–1810.
49 O. Enoki, H. Katoh and K. Yamamoto, *Org. Lett.*, 2006, **8**, 569–571.
50 O. Lytken, *EccentricXPS for free on Igor Exchange*, http://www.wavemetrics.com/project/EccentricXPS.
51 K. V. Klementiev, *XANES dactyloscope for Windows, freeware*, http://www.cells.es/Beamlines/CLAESS/software/xanda.html.
52 Z. Klencsár, E. Kuzmann and A. Vértes, *J. Radioanal. Nucl. Chem.*, 1996, **210**, 105–118.